

Three-dimensional and C-mode OCT imaging with a compact, frequency swept laser source at 1300 nm

R. Huber, M. Wojtkowski and J. G. Fujimoto

Department of Electrical Engineering and Computer Science
and Research Laboratory of Electronics,
Massachusetts Institute of Technology, Cambridge, MA 02139
Tel: 617-253-8920, Fax: 617-253-9611
rhuber@mit.edu

J. Y. Jiang and A. E. Cable

Thorlabs, Inc.
435 Route 206 North
Newton, NJ 07860

Abstract: We demonstrate high resolution, three-dimensional OCT imaging with a high speed, frequency swept 1300 nm laser source. A new external cavity semiconductor laser design, optimized for application to swept source OCT, is discussed. The design of the laser enables adjustment of an internal spectral filter to change the filter bandwidth and provides a robust bulk optics design. The laser generates ~30 mW instantaneous peak power at an effective 16 kHz sweep rate with a tuning range of ~133 nm full width. In frequency domain reflectometry and OCT applications, 109 dB sensitivity and ~10 μm axial resolution in tissue can be achieved with the swept laser. The high imaging speeds enable three-dimensional OCT imaging, including zone focusing or C-mode imaging and image fusion to acquire large depth of field data sets with high resolution. In addition, three-dimensional OCT data provides coherence gated *en face* images similar to optical coherence microscopy (OCM) and also enables the generation of images similar to confocal microscopy by summing signals in the axial direction. High speed, three-dimensional OCT imaging can provide comprehensive data which combines the advantages of optical coherence tomography and microscopy in a single system.

©2005 Optical Society of America

OCIS codes: (110.4500) Optical coherence tomography; (140.3600) Lasers, tunable

References and Links

1. D. Huang, E.A. Swanson, C.P. Lin, J.S. Schuman, W.G. Stinson, W. Chang, M.R. Hee, T. Flotte, K. Gregory, C.A. Puliafito, and J.G. Fujimoto, "Optical coherence tomography," *Science* **254**, 1178-1181 (1991).
2. E.A. Swanson, D. Huang, M.R. Hee, J.G. Fujimoto, C.P. Lin, and C.A. Puliafito, "High-Speed Optical Coherence Domain Reflectometry," *Opt. Lett.* **17**, 151-153 (1992).
3. W. Drexler, U. Morgner, F.X. Kartner, C. Pitris, S.A. Boppart, X.D. Li, E.P. Ippen, and J.G. Fujimoto, "In vivo ultrahigh-resolution optical coherence tomography," *Opt. Lett.* **24**, 1221-1223 (1999).
4. A.F. Fercher, C.K. Hitzenberger, G. Kamp, and S.Y. Elzaiat, "Measurement of Intraocular Distances by Backscattering Spectral Interferometry," *Opt. Commun.* **117**, 43-48 (1995).
5. G. Häusler and M.W. Lindner, "'Coherence radar" and "spectral radar"-new tools for dermatological diagnosis," *J. Biomed. Opt.* **3**, 21-31 (1998).
6. R. Leitgeb, M. Wojtkowski, A. Kowalczyk, C.K. Hitzenberger, M. Sticker, and A.F. Fercher, "Spectral measurement of absorption by spectroscopic frequency-domain optical coherence tomography," *Opt. Lett.* **25**, 820-822 (2000).

7. M. Wojtkowski, V.J. Srinivasan, T.H. Ko, J.G. Fujimoto, A. Kowalczyk, and J.S. Duker, "Ultra-high-resolution, high-speed, Fourier domain optical coherence tomography and methods for dispersion compensation," *Opt. Express* **12**, 2404-2422 (2004).
8. S.H. Yun, G.J. Tearney, J.F. de Boer, and B.E. Bouma, "Motion artifacts in optical coherence tomography with frequency-domain ranging," *Opt. Express* **12**, 2977-2998 (2004).
9. J. Zhang, W.G. Jung, J.S. Nelson, and Z.P. Chen, "Full range polarization-sensitive Fourier domain optical coherence tomography," *Opt. Express* **12**, 6033-6039 (2004).
10. M.A. Choma, A.K. Ellerbee, C.H. Yang, T.L. Creazzo, and J.A. Izatt, "Spectral-domain phase microscopy," *Opt. Lett.* **30**, 1162-1164 (2005).
11. B.H. Park, M.C. Pierce, B. Cense, S.H. Yun, M. Mujat, G.J. Tearney, B.E. Bouma, and J.F. de Boer, "Real-time fiber-based multi-functional spectral-domain optical coherence tomography at 1.3 μm ," *Opt. Express* **13**, 3931-3944 (2005).
12. F. Lexter, C.K. Hitzenberger, A.F. Fercher, and M. Kulhavy, "Wavelength-tuning interferometry of intraocular distances," *Appl. Opt.* **36**, 6548-6553 (1997).
13. B. Golubovic, B.E. Bouma, G.J. Tearney, and J.G. Fujimoto, "Optical frequency-domain reflectometry using rapid wavelength tuning of a Cr⁴⁺:forsterite laser," *Opt. Lett.* **22**, 1704-1706 (1997).
14. S.R. Chinn, E.A. Swanson, and J.G. Fujimoto, "Optical coherence tomography using a frequency-tunable optical source," *Opt. Lett.* **22**, 340-342 (1997).
15. S.H. Yun, G.J. Tearney, J.F. de Boer, N. Iftimia, and B.E. Bouma, "High-speed optical frequency-domain imaging," *Opt. Express* **11**, 2953-2963 (2003).
16. R. Huber, M. Wojtkowski, K. Taira, J.G. Fujimoto, and K. Hsu, "Amplified, frequency swept lasers for frequency domain reflectometry and OCT imaging: design and scaling principles," *Opt. Express* **13**, 3513-3528 (2005).
17. M.A. Choma, K. Hsu, and J. Izatt, "Swept source optical coherence tomography using an all-fiber 1300-nm ring laser source," *J. Biomed. Opt.* **10**, #044009 (2005).
18. J.F. de Boer, B. Cense, B.H. Park, M.C. Pierce, G.J. Tearney, and B.E. Bouma, "Improved signal-to-noise ratio in spectral-domain compared with time-domain optical coherence tomography," *Opt. Lett.* **28**, 2067-2069 (2003).
19. R. Leitgeb, C.K. Hitzenberger, and A.F. Fercher, "Performance of Fourier domain vs. time domain optical coherence tomography," *Opt. Express* **11**, 889-894 (2003).
20. M.A. Choma, M.V. Sarunic, C. Yang, and J. Izatt, "Sensitivity advantage of swept source and Fourier domain optical coherence tomography," *Opt. Express* **11**, 2183-2189 (2003).
21. M. Wojtkowski, R. Leitgeb, A. Kowalczyk, T. Bajraszewski, and A.F. Fercher, "In vivo human retinal imaging by Fourier domain optical coherence tomography," *J. Biomed. Opt.* **7**, 457-463 (2002).
22. N.A. Nassif, B. Cense, B.H. Park, M.C. Pierce, S.H. Yun, B.E. Bouma, G.J. Tearney, T.C. Chen, and J.F. de Boer, "In vivo high-resolution video-rate spectral-domain optical coherence tomography of the human retina and optic nerve," *Opt. Express* **12**, 367-376 (2004).
23. M. Wojtkowski, T. Bajraszewski, I. Gorczynska, P. Targowski, A. Kowalczyk, W. Wasilewski, and C. Radzewicz, "Ophthalmic imaging by spectral optical coherence tomography," *Am. J. Ophthalmol.* **138**, 412-419 (2004).
24. R.A. Leitgeb, L. Schmetterer, C.K. Hitzenberger, A.F. Fercher, F. Berisha, M. Wojtkowski, and T. Bajraszewski, "Real-time measurement of in vitro flow by Fourier-domain color Doppler optical coherence tomography," *Opt. Lett.* **29**, 171-173 (2004).
25. M.V. Sarunic, M.A. Choma, C.H. Yang, and J.A. Izatt, "Instantaneous complex conjugate resolved spectral domain and swept-source OCT using 3x3 fiber couplers," *Opt. Express* **13**, 957-967 (2005).
26. S.H. Yun, C. Boudoux, G.J. Tearney, and B.E. Bouma, "High-speed wavelength-swept semiconductor laser with a polygon-scanner-based wavelength filter," *Opt. Lett.* **28**, 1981-1983 (2003).
27. W.Y. Oh, S.H. Yun, G.J. Tearney, and B.E. Bouma, "Wide tuning range wavelength-swept laser with two semiconductor optical amplifiers," *IEEE Photonics Technol. Lett.* **17**, 678-680 (2005).
28. S.T. Sanders, J.A. Baldwin, T.P. Jenkins, D.S. Baer, and R.K. Hanson, "Diode-laser sensor for monitoring multiple combustion parameters in pulse detonation engines," *P. Combust. Inst.* **28**, 587-594 (2000).
29. S.T. Sanders, J. Wang, J.B. Jeffries, and R.K. Hanson, "Diode-laser absorption sensor for line-of-sight gas temperature distributions," *Appl. Opt.* **40**, 4404-4415 (2001).
30. J. Wang, S.T. Sanders, J.B. Jeffries, and R.K. Hanson, "Oxygen measurements at high pressures with vertical cavity surface-emitting lasers," *Appl. Phys. B* **72**, 865-872 (2001).
31. G. Totschnig, M. Lackner, R. Shau, M. Ortsiefer, J. Roskopf, M.C. Amann, and F. Winter, "1.8 μm vertical-cavity surface-emitting laser absorption measurements of HCl, H₂O and CH₄," *Meas. Sci. Technol.* **14**, 472-478 (2003).
32. A.A. Bol'shakov, B.A. Cruden, and S.P. Sharma, "Determination of gas temperature and thermometric species in inductively coupled plasmas by emission and diode laser absorption," *Plasma Sci. Technol.* **13**, 691-700 (2004).
33. L.A. Kranendonk, R.J. Bartula, and S.T. Sanders, "Modeless operation of a wavelength-agile laser by high-speed cavity length changes," *Opt. Express* **13**, 1498-1507 (2005).
34. W. Eickhoff and R. Ulrich, "Optical Frequency-Domain Reflectometry in Single-Mode Fiber," *Appl. Phys. Lett.* **39**, 693-695 (1981).
35. R. Passy, N. Gisin, J.P. Vonderweid, and H.H. Gilgen, "Experimental and Theoretical Investigations of Coherent OFDR with Semiconductor-Laser Sources," *J. Lightwave Technol.* **12**, 1622-1630 (1994).

36. U. Glombitza and E. Brinkmeyer, "Coherent Frequency-Domain Reflectometry for Characterization of Single-Mode Integrated-Optical Wave-Guides," *J. Lightwave Technol.* **11**, 1377-1384 (1993).
37. H. Barfuss and E. Brinkmeyer, "Modified Optical Frequency-Domain Reflectometry with High Spatial-Resolution for Components of Integrated Optic Systems," *J. Lightwave Technol.* **7**, 3-10 (1989).
38. F. Lexer, C.K. Hitzenberger, W. Drexler, S. Molebny, H. Sattmann, M. Sticker, and A.F. Fercher, "Dynamic coherent focus OCT with depth-independent transversal resolution," *J. Mod. Opt.* **46**, 541-553 (1999).
39. A. Divetia, T.H. Hsieh, J. Zhang, Z.P. Chen, M. Bachman, and G.P. Li, "Dynamically focused optical coherence tomography for endoscopic applications," *Appl. Phys. Lett.* **86**, #103902 (2005).
40. M.J. Cobb, X.M. Liu, and X.D. Li, "Continuous focus tracking for real-time optical coherence tomography," *Opt. Lett.* **30**, 1680-1682 (2005).
41. B. Qi, A.P. Himmer, L.M. Gordon, X.D.V. Yang, L.D. Dickensheets, and I.A. Vitkin, "Dynamic focus control in high-speed optical coherence tomography based on a microelectromechanical mirror," *Opt. Commun.* **232**, 123-128 (2004).
42. Y.M. Wang, Y.H. Zhao, J.S. Nelson, Z.P. Chen, and R.S. Windeler, "Ultrahigh-resolution optical coherence tomography by broadband continuum generation from a photonic crystal fiber," *Opt. Lett.* **28**, 182-184 (2003).
43. K. Bizheva, A. Unterhuber, B. Hermann, B. Povazay, H. Sattmann, A.F. Fercher, W. Drexler, M. Preusser, H. Budka, A. Stingl, and T. Le, "Imaging ex vivo healthy and pathological human brain tissue with ultrahigh-resolution optical coherence tomography," *J. Biomed. Opt.* **10**, (2005).
44. Y.T. Pan, Z.G. Li, T.Q. Xie, and C.R. Chu, "Hand-held arthroscopic optical coherence tomography for in vivo high-resolution imaging of articular cartilage," *J. Biomed. Opt.* **8**, 648-654 (2003).
45. Y. Zhang, J.T. Rha, R.S. Jonnal, and D.T. Miller, "Adaptive optics parallel spectral domain optical coherence tomography for imaging the living retina," *Opt. Express* **13**, 4792-4811 (2005).
46. J.A. Izatt, M.R. Hee, G.M. Owen, E.A. Swanson, and J.G. Fujimoto, "Optical Coherence Microscopy in Scattering Media," *Opt. Lett.* **19**, 590-592 (1994).
47. J.A. Izatt, M.D. Kulkarni, H.W. Wang, K. Kobayashi, and M.V. Sivak, "Optical coherence tomography and microscopy in gastrointestinal tissues," *IEEE J. Sel. Top. Quantum Electron.* **2**, 1017-1028 (1996).
48. A.D. Aguirre, P. Hsiung, T.H. Ko, I. Hartl, and J.G. Fujimoto, "High-resolution optical coherence microscopy for high-speed, in vivo cellular imaging," *Opt. Lett.* **28**, 2064-2066 (2003).
49. S.L. Jiao, R. Knighton, X.R. Huang, G. Gregori, and C.A. Puliafito, "Simultaneous acquisition of sectional and fundus ophthalmic images with spectral-domain optical coherence tomography," *Opt. Express* **13**, 444-452 (2005).
50. M. Wojtkowski, V. Srinivasan, J.G. Fujimoto, T. Ko, J.S. Schuman, A. Kowalczyk, and J.S. Duker, "Three-dimensional retinal imaging with high-speed ultrahigh-resolution optical coherence tomography," *Ophthalmology* **112**, 1734-1746 (2005).
51. P.I. Richter and T.W. Hänsch, "Diode-Lasers in External Cavities with Frequency-Shifted Feedback," *Opt. Commun.* **85**, 414-418 (1991).
52. J.J. Snyder, "Paraxial Ray Analysis of a Cats-Eye Retroreflector," *Appl. Opt.* **14**, 1825-1828 (1975).
53. S.H. Yun, G.J. Tearney, B.E. Bouma, B.H. Park, and J.F. de Boer, "High-speed spectral-domain optical coherence tomography at 1.3 μ m wavelength," *Opt. Express* **11**, 3598-3604 (2003).

1. Introduction

Optical Coherence Tomography (OCT) [1] has found widespread applications for cross sectional imaging of tissue *in situ* with micron scale resolution. Earlier OCT systems were based on time domain detection where echo time delays of light detected by measuring the interference signal as a function of time, while scanning the optical path length of the reference arm.[2, 3] Recently, OCT techniques based on Fourier domain detection have become an active area of research.[4-11] OCT with Fourier domain detection uses either a spectrograph [4, 5] or a frequency swept laser source [4, 12-17] to measure echo time delays of light by spectrally resolving the interference signal. The magnitude and time delay of the backscattered light is reconstructed by Fourier transformation of the fringe signal versus frequency. Recent studies have shown that Fourier domain detection using spectrometers or frequency swept lasers can dramatically improve the detection sensitivity and enable significantly higher scan speeds than standard time domain detection techniques.[18-20] In contrast to OCT imaging at wavelengths near 800 nm where OCT systems using spectrometer based Fourier domain detection are widely applied, [7, 21-25] Fourier domain detection using frequency swept light sources are especially important for imaging in the 1300 nm wavelength range, where low cost CCDs are not available. The application of frequency swept light sources for OCT imaging also enables dual balanced detection, reducing the need for high

dynamic range A/D conversion and eliminating the need for high performance spectrometers and CCDs. For this reason, there is considerable interest in the development of high speed, frequency swept light sources for OCT, as well as new scanning protocols which make use of the higher acquisition speed.[15, 16, 26, 27] In addition to the promising perspective for OCT imaging, rapidly tunable or frequency swept light sources with broad tuning ranges have many other applications in fields like spectroscopy [28-33] or photonic device and waveguide characterization.[34-37] In all of these applications, the narrow band, tunable laser provides spectral encoding in time and the spectral information is recorded by the transient signal while the laser is tuned.

Investigations of the laser dynamics of frequency swept laser sources have shown that short cavity lengths improve performance.[16] Bulk optics laser designs are attractive because short cavity lengths are usually easier to achieve than in fiber laser designs. In this manuscript, we demonstrate a compact, high power, high speed, frequency swept laser light source at 1300 nm for three-dimensional OCT imaging. The short cavity length design provides good performance, high compactness and high stability. In addition, the cavity design enables adjustment of the intra-cavity filter bandwidth, providing direct control of the instantaneous coherence length. The laser achieves an effective bi-directional sweep rate of 16 kHz using an 8 kHz frequency sweep waveform, with a peak output power of ~30 mW and an instantaneous spectral width of ~0.17 nm. The laser achieves a bandwidth of 133 nm full width, yielding an axial resolution of ~10 μm in tissue. The design of this novel cavity layout is discussed in detail.

Time domain OCT imaging using two-dimensional zone focusing and image fusion or focus tracking to increase the depth of view has been demonstrated, but suffers from slow data acquisition speeds.[3, 38-41] The high data acquisition speed of swept source OCT makes it possible to acquire images with enhanced depth of field in a fraction of a second by C-mode imaging, fusing together multiple images with different focal depths, as demonstrated in two-dimensional, time domain OCT.[3] Full, three-dimensional data sets with enhanced depth of field can be acquired within several seconds by acquiring and fusing multiple three-dimensional data sets with different focus depths. This overcomes depth of field limitations which are normally associated with the small focused spot sizes required for high transverse resolution.

A second approach for increasing the depth of focus while maintaining high transverse resolution is the technique of "dynamic focusing" where the depth of the focal plane is moved synchronously with the depth of the coherence gate.[38-45] In OCT using Fourier domain detection, axial scan rates are typically in the range of tens of kilohertz or higher and dynamic focusing is not possible due to limitations in the adjustment speed of the focus depth. An alternate approach which overcomes this limitation is to acquire entire three-dimensional sets of data and fuse them to one large volume data set. The total acquisition time will be longer than for dynamic focusing, however the higher acquisition speed of swept source OCT compared to time domain OCT in part compensates for this time increase.

Three-dimensional OCT data provides coherence gated *en face* images similar to optical coherence microscopy (OCM) and also enables the generation of images similar to confocal microscopy. Coherence gated *en face* images similar to optical coherence microscopy (OCM) can be generated by extracting and displaying signals within the coherence gate at a constant depth in the three-dimensional data.[46-48] Images similar to confocal microscopy can be generated by summing the three-dimensional data in the axial direction. This removes the coherence gating effect and the depth gating is provided only by the confocal gate. Similar methods for generating *en face* images have been used to produce OCT fundus images in ophthalmic OCT.[7, 49, 50] These results demonstrate that high speed, three-dimensional OCT combines the functions of optical coherence tomography and microscopy in a single instrument.

2. Experimental setup

2.1 Laser design

Figure 1 shows a schematic representation of the frequency swept, external cavity laser system. Starting from the left side of the figure: The semiconductor gain element (1) is approximately 1 mm in length, with an estimated index of refraction of 3.5 at 1300 nm. The left facet serves as the output coupler for the laser and the output facet reflectivity is estimated to be 15 %. The semiconductor gain element is bonded to a TE cooler and is maintained at approximately 22° C.

The intra-cavity side of the semiconductor gain element utilizes a curved waveguide and an anti-reflection (AR) coated facet with an estimated effective intra-cavity facet reflectivity of approximately 10⁻⁴, which suppresses self-lasing and allows the semiconductor element to serve as an effective gain medium for the external cavity. The collimating lens is an AR coated aspheric lens (2) with a 2 mm focal length. A free space region of approximately 370 mm between the collimating aspheric lens and the grating is used to adjust the overall length of the cavity. The diffraction grating (3) has 1017 lines/mm and is mounted on a resonant galvanometer scanner (Electro-Optical Products Corp.) that provides a total optical angular displacement of approximately 14 degrees at 8 kHz. After the grating there is a 45 mm focal length achromatic doublet lens (4) which was optimized for 1.0 μm, 1.3 μm and 1.5 μm wavelengths. The lens focuses different spectral components onto a high reflecting end mirror (5). A slit with 10 μm width (6), bonded directly onto the reflective surface of a broadband dielectric mirror (5) provides active wavelength selection. Only light within a certain wavelength bandwidth, such that it is focused on the slit, will be reflected by the end mirror. The end mirror is placed at the back focal plane of the doublet lens and has a reflectivity of greater than 98.5 %. The end mirror and slit assembly act as the back-reflector of the laser resonator. Light output from the laser is collimated by an AR coated aspheric lens with a focal length of 0.7 mm (not shown in Fig. 1) and directed through a -55 dB optical isolator that prevents feedback into the laser cavity. An AR coated, 4 mm focal length aspheric lens is then used to couple the light into an AR coated, single mode fiber.

The laser system is frequency swept by tilting the grating via the resonant scanner shown in Fig. 1. The laser dynamics can be understood by considering the situation where a single longitudinal mode is lasing within the cavity. If the rotation axis of the grating is perpendicular to the optical axis, the cavity length is kept substantially constant when the grating is tilted.

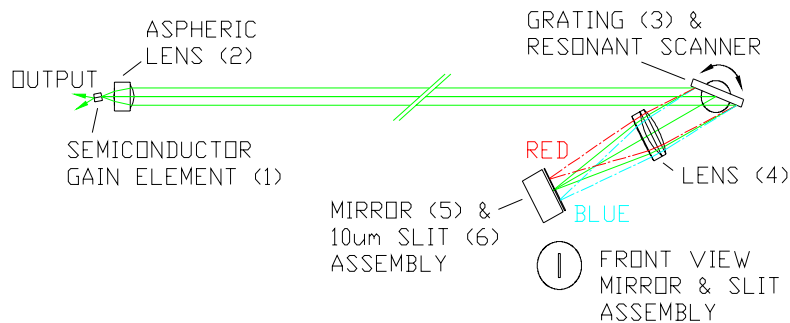


Fig. 1. Schematic diagram of the high speed, frequency swept laser system. The resonant scanner and grating assembly sweep the various wavelengths across the reflective slit, thereby tuning the laser while maintaining a constant cavity length.

Hence, there is no wavelength change within the cavity for very small rotations of the grating, once the rotation is sufficient to ensure that the next longitudinal mode has lower loss, the laser will hop to this next mode. The center frequency of the laser is consequently shifted by one longitudinal cavity mode, which is given by the free spectral range of the cavity

(330 MHz). Further rotation of the grating leads to this pattern repeating itself, whereby the laser wavelength as a function of grating angle follows a “staircase” shaped tuning curve. In reality, the finite width of the filter function allows many longitudinal modes, approximately 80 for this cavity configuration, to lase simultaneously. Therefore, the laser generates a comb of frequencies that tune in a stepwise fashion, with the step size being equal to the longitudinal mode spacing.

As shown in ref. [33], varying the cavity length at high speeds produces operation that is similar to the operation of a frequency shifted feedback laser.[51] A value R is defined as the relative frequency change of the cavity modes with respect to their free spectral range during one optical roundtrip. The laser in ref. [33] tunes in a modeless regime with a value $R \gg 0.05$ using a rapid change in cavity length, however the laser presented here tunes with distinct cavity modes. For the cavity layout in Fig. 1 there is no change in the geometrical cavity length while the laser is tuned, so R is substantially 0. This should provide an optimum build up time for a mode structure, which has been demonstrated to provide a higher output power stability.[33] In contrast to spectroscopic applications, where a smooth and continuous spectral density is often required [33], for swept source OCT applications a discrete frequency spectrum is acceptable, provided the overall bandwidth is sufficiently narrow. A number of other cavity designs were explored with non-zero values of R and compared to the design presented here. These designs had similar layout with the same sequence of components, however with different cavity lengths. In each instance, the instantaneous coherence length was found to be considerably shorter than for the design shown here. To estimate the coherence properties of the source, the fringe contrast was measured when the output was coupled into a Michelson interferometer. The amplitude of the fringe signal was measured as a function of the interferometer arm length difference. We observed a 3 dB drop over about 3.5 to 4 mm arm length difference in the Michelson interferometer. This corresponds to a coherence length of 14 to 16 mm, accounting for the symmetry around zero delay when both positive and negative arm length differences are considered. A more accurate measurement of the dynamic coherence properties relevant for OCT is given in the following sections. The coherence length for the static case when the laser is not frequency scanned is determined by measuring the spectral linewidth of the output with an optical spectrum analyzer. A resolution limited static linewidth of < 0.02 nm was measured and corresponds to > 2 cm arm length difference in a Michelson interferometer or to > 8 cm coherence length.

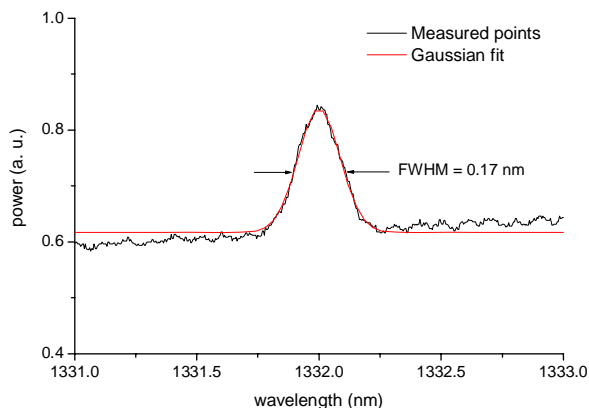


Fig. 2. Amplified spontaneous emission (ASE) spectrum of the cavity at an injection current below the laser threshold, showing the approximate filter function provided by the grating, slit and end mirror.

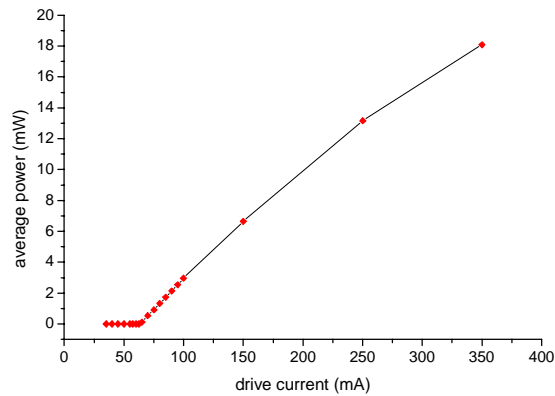


Fig. 3. Output power vs. injection current of the laser. The laser threshold is 63 mA at a diode temperature of 22 °C.

In addition to providing constant cavity length with tuning, the design also provides robustness to misalignment because it uses a cat's eye configuration at the end mirror. This configuration can provide superior stability over designs with a quasi-collimated beam on the end mirror, enabling better long term stability.[52] A further advantage of the design is the ability to change the filter function using different slit widths. Spatial filtering is performed by the slit in the Fourier-plane, analogous to a spectrometer so that cavity alignment is preserved. In addition to a fixed slit, it is also possible to use an adjustable slit. The performance characterization discussed in the following section is based on a 10 μm wide slit, Fig. 1(6), which corresponds approximately to the minimum filter width which can be achieved without excessively reducing the backcoupling efficiency. Figure 2 shows the output spectrum of the laser well below the lasing threshold. The spectrum contains signal from the direct ASE and ASE from one roundtrip through the cavity.

The peak structure in Fig. 2 represents the additional light intensity backcoupled from the cavity and gives a measure of the filter function for one roundtrip. The 10 μm wide slit gives an approximate filter bandwidth of 0.17 nm. Care was taken to ensure that the FWHM of the filter function did not change appreciably as the current was increased from below threshold to the 45 mA used for this measurement. The laser threshold current was measured to be 63 mA (Fig. 3).

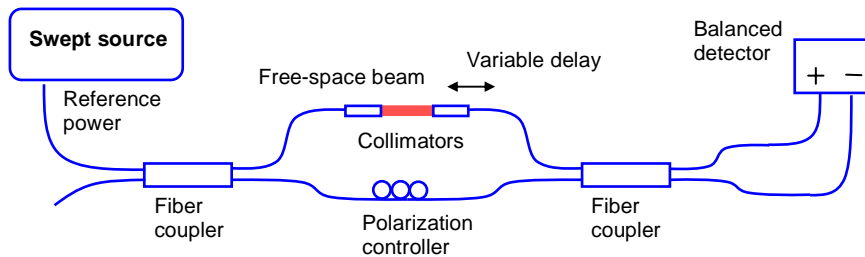


Fig. 4. Dual balanced Mach-Zehnder interferometer for the generation of a clock signal.

2.2 *k-space clock*

Figure 4 shows a schematic of the *k-space clock* that was used to resample the OCT data to equally spaced points in frequency. This signal is generated using a Mach-Zehnder interferometer (MZI), with both output ports recorded in dual balanced detection mode. The signal from the differential receiver shows a sinusoidal oscillation over time with varying frequency according to the non-linearity of the frequency sweep. All peaks as well as the zero crossings recorded during the sweep are equally spaced in frequency and are used with a fast “next neighbour check algorithm” [16] for OCT imaging. The differential detection scheme reduces the non-interferometric terms as well as the intensity noise to give a stable clock signal. A trigger signal with adjustable frequency can be generated by adjusting the free space beam path in the MZI.

2.3 *OCT imaging setup*

The OCT system is shown in Fig. 5. The system uses a circulator and dual balanced detection scheme. The photodiodes have a bandwidth of 80 MHz and a transimpedance gain of $\sim 50,000$ V/A (New Focus, model 1817). A responsivity of ~ 0.8 A/W was estimated at 1300 nm from the given value of 1 A/W at a wavelength of 1550 nm. The fringe signal from the OCT interferometer is acquired on one channel of a two channel, high speed analog to digital converter (A/D) operating up to 100 Msamples/s with 14 bit resolution (National Instruments, model NI5122).

Two approaches for real time recalibration of the instantaneous wavelength to frequency have been tested. In the first approach, a fraction of the laser output power is split off into fiber Fabry Perot filter (FFPI, Micron Optics Inc.) with a free spectral range (FSR) of 50 GHz (0.28 nm). A 125 MHz bandwidth photodetector (New Focus, model 1811) records the transmitted comb-like signal when the laser is frequency swept. Each peak in the recalibration signal corresponds to a frequency shift of 50 GHz, one FSR, with respect to the previous peak correlating to the transmission maxima of the FFPI. After electronic filtering, a sinusoidal signal is generated.

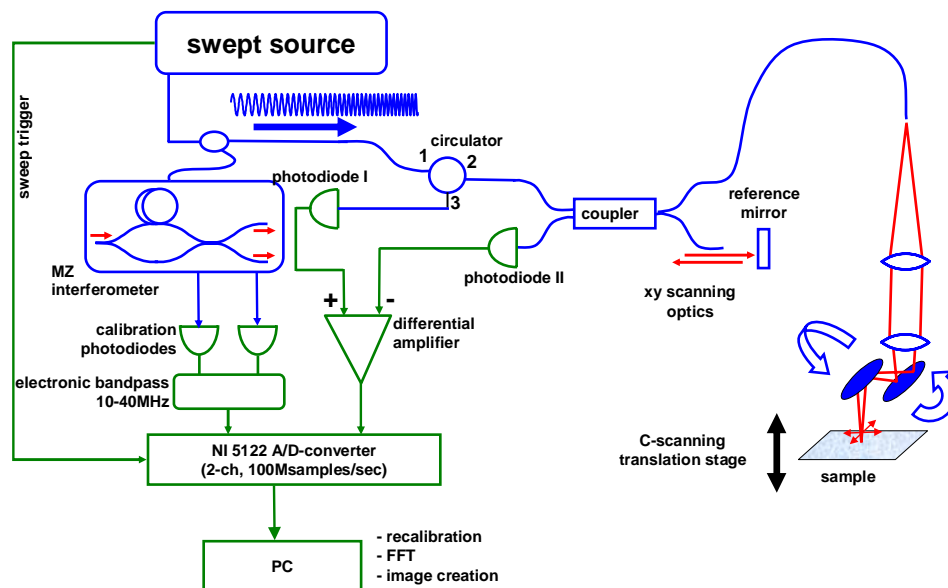


Fig. 5. Schematic of the swept source OCT system using C-mode scanning (optics: blue; electronics: green).

In the second approach for recalibration, a fraction of the laser power was tapped off and coupled into one input port of an unbalanced Mach-Zehnder interferometer (MZI), described above. A 100 MHz bandwidth, dual balanced photodetector (Thorlabs, model PDA10B1) at the two output ports of the MZI provides a sinusoidal fringe signal, where zero crossings as well as maxima and minima are evenly spaced in frequency.

This approach enables an arbitrary adjustment of the fringe frequency by changing the unbalanced path length in the MZI. A second advantage of the MZI is that it is less sensitive to small frequency tuning discontinuities and noise than the FFPI and produces a lower noise output signal which does not require bandpass filtering. Electronic filtering can introduce phase changes of the fringe signal over frequency, especially when large sweep ranges and speeds are covered. This effect leads to miscalibration, affecting imaging performance at large depths. Figure 5 shows the experimental configuration where the MZI without a bandpass filter is used to obtain the recalibration signal. When the FFPI is used for recalibration instead of the MZI, the electronic bandpass is inserted as indicated in Fig. 4. The images in Fig. 9 were acquired with the MZI recalibration signal. The MZI was set for 6 mm difference in optical path lengths. All other images were acquired with the FFPI recalibration signal.

In both recalibration approaches the output of the single channel detector (FFPI) or the dual balanced detector (MZI) are recorded on the second channel of the A/D simultaneously with the signal from the OCT interferometer. This enables real time recalibration of the interference signal for equal spacing in frequency prior to the FFT algorithm. The fast “next neighbour check” algorithm applied for realtime recalibration is discussed in detail in reference [16] and was applied not only for fast, real time preview, but also for the data sets and images.

For two-dimensional OCT imaging, the data acquisition is done in the following sequence: The A/D-card is triggered by a TTL signal generated by the driver of the resonant galvanometer scanner and digitization is performed at 50 MHz for one sweep. One A/D channel is used to acquire the signal and the second is used to acquire the recalibration signal. This data set is one record on the on-board buffer of the A/D card and contains information on one axial scan. Typically 1400 points are acquired for the signal as well as for the recalibration signal for one axial scan. 3500 such records are stored on the onboard buffer of the card, representing one OCT image and then transferred to the PC memory. In the PC, each individual record from the sample signal is recalibrated to an equidistant spacing in frequency by the next neighbour check algorithm [16], only points from the sample trace are selected which correspond to a maximum or a minimum in the calibration signal. The recalibrated data set typically consists of 800 points. This data set is zero padded up to 1024 points and then Fourier transformed. Therefore, one axial scan in the image consists of 512 pixels. Different parameters were used, depending upon the application; however the sequence of data processing was the same as described above.

OCT imaging is performed by using a beam scanning microscope consisting of a 40 mm focal length, NA = 0.14 fiber collimating lens and a 20 mm focal length, NA = 0.26 objective lens. A 6 mm aperture XY galvanometer scanner was used for post objective beam scanning. The calculated transverse spot size is $4.5 \mu\text{m}$ (modefield diameter $2w_0$ at $1/e^2$). At a center wavelength of $\lambda_0 = 1350 \text{ nm}$, the calculated confocal parameter $b = 2z_R = \frac{2\pi w_0^2}{\lambda}$ is $25 \mu\text{m}$ in air, where the Rayleigh length is z_R and the beam radius w_0 . The spotsize is chosen such that a nearly symmetric voxelsize of about $5 \times 5 \times 10 \mu\text{m}$ in tissue is achieved. Despite the depth gating effect from the short confocal parameter, the additional coherence gating effect of OCT provides a decisive advantage in imaging capability because the coherence gate is much more effective than the confocal gate on a log scale. The axial zone focusing was performed using a translation stage in Z-direction. Full, three-dimensional data subsets were acquired before readjusting the axial focal depth.

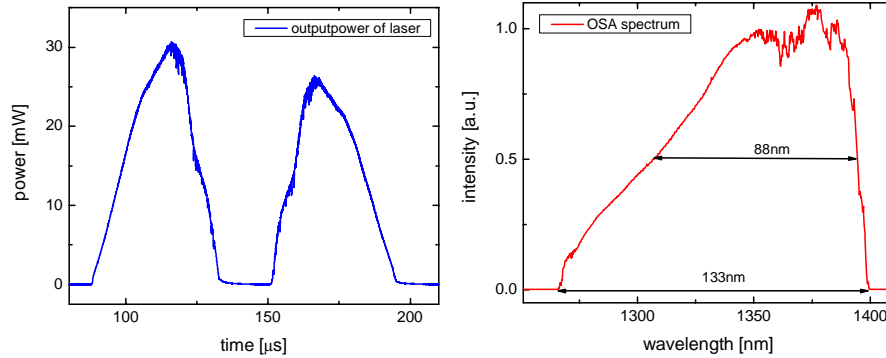


Fig. 6. Left: Transient intensity profile of the sweep for a forward and a backward scan. Right: Integrated spectrum of swept laser source.

The data acquisition was performed in a burst transfer mode to minimize limitations from the speed of the PCI bus as well as trigger rearming times and data transfer initialization lags of the A/D card. Depending on the image size, about 10 frames could be stored in the 32 MB onboard buffer, which were then transferred as one data block to the system memory. Larger data sets could be acquired if a larger onboard buffer would be used or if A/D designs were available which would enable high-speed, direct data transfer to the system memory. Both forward and backward scans were acquired, resulting in a maximum image acquisition rate of 32 frames per second with 512 transverse pixels (axial scans) per image.

3. Performance of the frequency swept laser source for OCT imaging

The important parameters of a swept laser source for OCT applications include the spectral width of the sweep, output power, achievable sensitivity and instantaneous linewidth. Figure 6(left) shows the transient intensity profiles of the laser for a forward (shorter to longer wavelengths) and a backward (longer to shorter wavelengths) sweep. The slightly different peak powers of the sweeps can be attributed to nonlinear effects in the gain chip, which favor a downshift in energy.[16, 26] The 30 mW maximum output power compares well with the maximum output power achieved in the non-scanned case, suggesting that the laser is operating in saturation even at this high sweep speed. The short cavity length of 45 cm provides a sufficient number of roundtrips at each spectral position for build up of laser emission, even in the dynamic frequency scanned regime.[16]

Figure 6(right) depicts the integrated spectrum of the laser source measured with an optical spectrum analyzer. A full width of 133 nm is achieved with slight asymmetry. The full width at half maximum (FWHM) is ~88 nm. A Gaussian spectrum with an 88 nm FWHM would correspond to an OCT resolution (amplitude) of 8.5 μm in air. The actual FWHM-resolution of the point spread function (PSF of the FFT amplitude) was measured to be 12.6 μm in air for the backward scan and 16.1 μm for the forward scan (Fig. 7).

The discrepancy of these values compared to the theoretical resolution can be attributed to the over pronounced wings of the integrated spectrum caused by the nonlinear frequency sweep, the non-Gaussian shape of the spectrum, errors in the recalibration procedure, as well as a slightly narrower effective spectral width of the actual data set used to calculate the PSF. The asymmetric shape of the PSF in the forward scan might be due to a non-uniform distribution of calibration errors over the sweep. These resolution measurements suggest an effective axial resolution in tissue of about 9 μm and 12 μm for backward and forward scan, respectively. The reason for the difference of forward and backward scan will be discussed in the next paragraph.

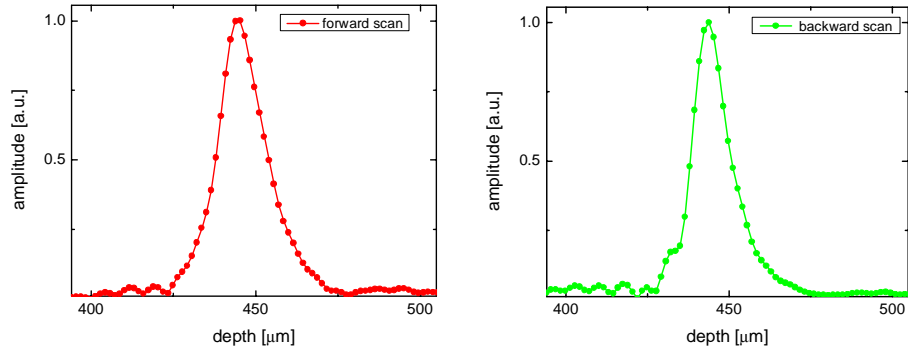


Fig. 7. Left: Point spread function (PSF) in OCT application for a forward scan - resolution in air $16 \mu\text{m}$ (FWHM of amplitude) corresponding to $12 \mu\text{m}$ in tissue. Right: PSF for a backward scan - resolution in air $12 \mu\text{m}$ (FWHM of amplitude) corresponding to $9 \mu\text{m}$ in tissue.

To characterize the sensitivity of the laser source in OCT measurements, a calibrated, -47 dB reflection from a mirror was used. The sensitivity measurements were performed using a simplified sample arm without the OCT imaging optics. The reference arm power was attenuated to several tens of micro-Watts average power. Optimum sensitivity performance could be obtained over more than one order of magnitude variation in reference arm power, before the heterodyne gain became too small, or the excess noise too large. For these measurements, the A/D card was operated at 100 Msamples/s . After recalibration, the data set consisted of about 810 points. Prior to Fourier transformation the data set was zero padded to 8192 points, resulting in 4096 depth points after Fourier transformation.

The sensitivity values were measured by taking the ratio between the peak of the amplitude of the PSF after Fourier transformation and the standard deviation of the noise floor measured with the sample arm blocked. The quoted dB values are 20 times the decadic logarithm of this ratio. System losses of $\sim 5 \text{ dB}$ arising from losses in the optics and mirror reflectivity were subtracted from the measured sensitivity values. The measured maximum sensitivity values at short delays were 109 dB and 108 dB with 6 mW and 7 mW peak power on the sample for the backward and forward sweeps, respectively. The average power on the sample for the sensitivity measurements was 2.8 mW . The measured values of sensitivity agree well with the calculated shot noise limit of 111 dB and 112 dB for the experimental parameters, a detection bandwidth of 50 MHz , detector efficiency of 0.85 e/photon , Gaussian spectral shape and 800 sampling points (see Reference [20]).

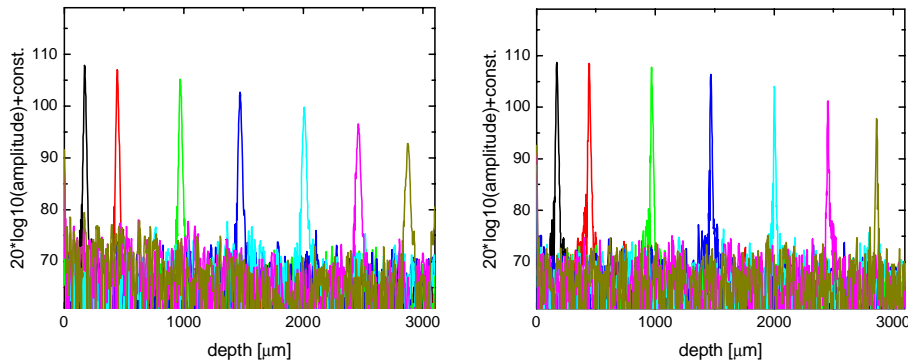


Fig. 8. Measured PSFs in OCT application on a logarithmic scale for different delays relative to the reference arm length. The scale is adjusted by a constant such that the peak values reflect the sensitivity values at the different depth positions. Left: PSFs for backward scans. Right: PSFs for forward scans.

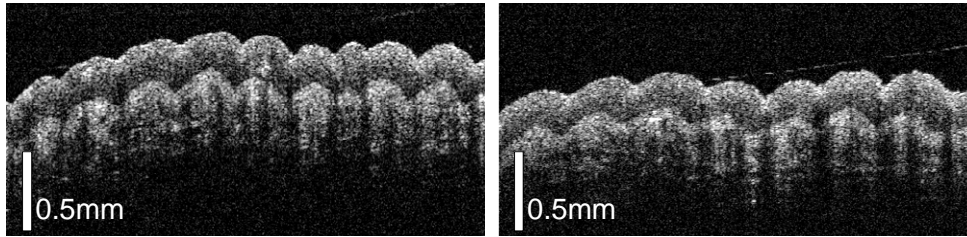


Fig. 9. Images of a human finger in vivo (3 mm x 1.5 mm) using forward sweeps only (left) and backward sweeps only (right).

Figure 8 shows the fall off in sensitivity versus scan depth which is typical for OCT imaging with Fourier domain detection.[16, 20-22, 53] The fall off in sensitivity with depth in swept source OCT can be attributed to the limited instantaneous coherence length, which produces a loss of fringe contrast as well as an increasing number of phase discontinuities in the interferometric fringe trace. These phase discontinuities produce a reduction in the PSF maxima with depth which occurs faster than the decrease in fringe visibility with depth. In these studies, a decrease of ~10 dB and ~15 dB over a depth range of 3 mm was observed for the backward and the forward sweeps, respectively.

The reason that the sensitivity decreases faster for the forward sweep may be because of the nonlinearities in the gain medium, which can more effectively broaden the spectrum when the laser intracavity filter is swept in the direction of lower energy. For the backward sweep, the filter is swept in the direction opposite the energy shift produced by the gain nonlinearity, producing a narrower spectrum. For delays up to 2 mm and 2.5 mm, the sensitivity values are above 100 dB for backward and forward scan respectively, providing sufficient SNR for most OCT imaging applications in highly scattering tissue. The PSFs for the forward sweeps show slightly broader wings on a logarithmic scale compared to the PSFs for the backward sweeps. This is consistent with the wider FWHM of the PSF for the forward and the backward sweep mentioned previously.

In order to characterize the differences in imaging performance for forward and backward scans, we analyzed two OCT images of a human finger in vivo obtained by using forward scans only (Fig. 9(left)) and backwards scans only (Fig. 9(right)). These results show that there is no significant difference in imaging quality and therefore both forward and backward sweeps can be used for imaging in most applications.

4. High speed swept source OCT imaging and three-dimensional zone focus OCT

The application of the frequency swept light source for high speed, swept source OCT imaging is demonstrated in Figs. 10-13. OCT imaging was performed with axial scan rates of 16 kHz using both forward and backward sweeps generated by the 8 kHz periodic drive. The average power on the sample was 1.4 mW. The A/D sampling rate was 50 Msamples/s. The axial image resolution was ~10 μm in tissue and the transverse spot size was ~4.5 μm . The depth of field, as defined by two times the Rayleigh range was $2z_R = \sim 25 \mu\text{m}$ in air, corresponding to ~35 μm in tissue.

Two different scanning protocols were used for two-dimensional, cross-sectional imaging and for three-dimensional, volumetric imaging. For acquiring single cross-sectional images, 3500 interference signal sweeps (axial scans) with 800 points equally distributed in optical frequency (number of points after recalibration) were acquired. The number of axial pixels is determined by the frequency spacing of the recalibration signal and the spectral bandwidth of the laser source. The interference signal is zero padded up to a power of 2 to increase the number of samples to 512 points (1024 points before FFT), enabling a more effective FFT algorithm. The resulting OCT image after zero padding and FFT consists of 3,500 transverse axial scans with 512 axial points per axial scan. Due to limitations in the performance of the

A/D converter, including trigger rearming time and on board buffer capacity, different data acquisition parameters were used for three-dimensional imaging. For three-dimensional, volumetric OCT imaging, 150 OCT cross-sectional images were acquired consisting of 512 axial scans (transverse pixels) with 256 axial points (axial pixels) per axial scan. Two-dimensional images are collected within 0.22 s. Three-dimensional data sets of 150 cross-sectional images with 512 axial scans each were collected within 6 seconds with 75% duty cycle. The ratio of this average axial scan acquisition rate to the laser sweep rate can be sustained for data-sets larger than the onboard buffer of the A/D-converter card. The limitation in the duty cycle was caused by the limited onboard memory buffer in the A/D converter board. The A/D card used in this study required a long record initialization time which precluded direct streaming of the data points to PC system memory. A duty cycle of 100% can be achieved by using a larger on-board memory buffer or by using an A/D converter board with a shorter record initialization time. In the OCT images shown, the DC level was suppressed sufficiently by dual balancing and no additional background subtraction was required. All images were recalibrated with the fast “next neighbour check” algorithm.[16]

OCT imaging was performed *in vivo* on the *Xenopus laevis* tadpole, a commonly used developmental biology specimen for investigations of organogenesis. The tadpole was anesthetized by 0.03% solution of MS-222 (tricaine methanesulfonate (TMS) ethyl 14-aminobenzoate). All animal handling was performed according to protocols approved by the M.I.T. Committee on Animal Care (CAC).

Figure 10 shows an example of three-dimensional swept source OCT imaging of a *Xenopus laevis* tadpole. OCT imaging was performed in a 1 mm x 1 mm region localized close to the gill structures. The region of interest is indicated on the microscope image (Fig. 10(a)). In order to demonstrate advantages of three-dimensional, volumetric OCT imaging, a three-dimensional data set was used to reconstruct 256 cross sectional, *en face* plane images. These planes are oriented perpendicular to the original OCT images and are equivalent to the planes imaged in optical coherence microscopy (OCM). The movie in Figure 10b demonstrates *en face* cross-sectional imaging. Each image consists of 512 horizontal pixels by 150 vertical pixels and represents a $\sim 10 \mu\text{m}$ thick slice as defined by the coherence gate in the axial direction. Summing the set of all of these *en face* images gives an image similar to that obtained by a confocal scanning laser microscope (CSLM) (Fig. 10(c)).

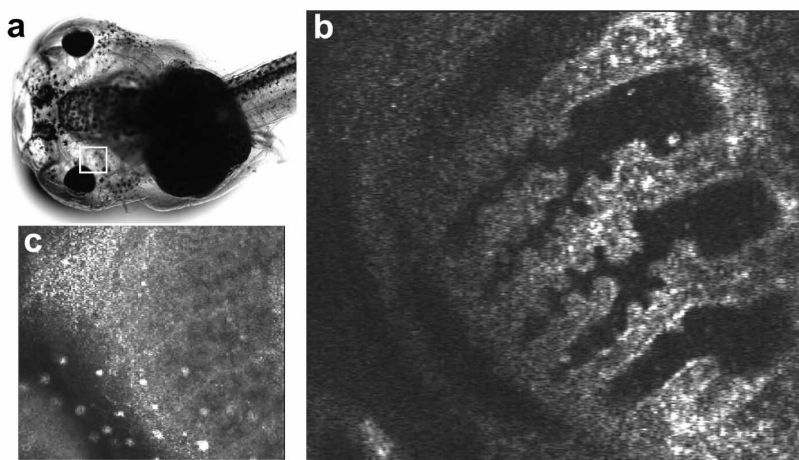


Fig. 10. (2MB movie) Application of high speed, swept source OCT for OCM imaging of African frog (*Xenopus laevis*) tadpole. Images show the gill region: a. Standard microscope image of the tadpole, the region imaged by OCT is marked as a white square; b. Movie showing consecutive *en face* images reconstructed from a three-dimensional OCT data set ([6MB version](#)); c. OCT “confocal” image obtained by integrating *en face* cross-sectional OCT images in the axial direction. The *en face* images b and c show a 1 mm x 1 mm field of view.

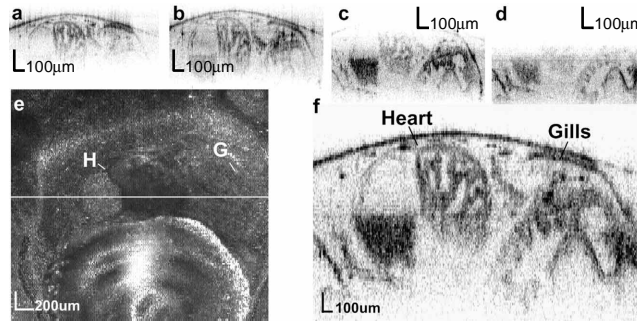


Fig. 11. C-mode, swept source OCT *in vivo* imaging of an African frog tadpole (*Xenopus laevis*) a-d. OCT images recorded with different focal depths; e. OCT "confocal" image obtained by summing of all *en face* sections in the axial dimension, white line indicates the position of the cross-sectional image that is displayed; f. Cross-sectional OCT image with extended depth of field obtained by fusing images a-d; H-heart and G-gills in the developing tadpole.

In this case, the axial resolution is approximately $\sim 35 \mu\text{m}$ as determined by the confocal parameter or depth of field. The reduced resolution of the axial gating in the CSLM-like image obscures detailed structures which can clearly be identified in the OCM images (Fig. 10(b)).

It should be pointed out that typical CSLMs use a higher NA and have a smaller spot size and a shorter confocal parameter than used in this study and therefore would provide a better confocal depth gating than shown here. At the same time, CSLMs require high NA focussing in order to achieve this confocal gating, while OCM can achieve axial gating using coherence and does not require high NA focusing. Although OCT and OCM resolutions are not as fine as standard CSLM, imaging is possible with larger working distance and wider field of view.

Figures 11-13 demonstrate the application of high speed, swept source OCT for C-mode imaging. An enhanced axial depth of field is obtained by acquiring multiple images with different focal positions of the objective lens. These images are then fused to create a single cross-sectional image with an extended depth of field. Figure 11a-d shows OCT cross-sectional images measured with four different focal depths. The confocal parameter limits the depth of field, since only backscattered light from the focal region is effectively coupled back into the OCT system. For axial depths which are out of the focal plane, the image contrast decreases and structures cannot be visualized. To increase the depth of field, the four OCT images were fused into a single image with an extended depth of field (Fig. 11(f)). The enhanced depth of field covers an axial range of about 0.6 mm. Figure 11e shows an *en face* image generated by summing the axial signals in the three-dimensional OCT data set. This image is similar to a confocal microscope image and enables precise registration of the individual OCT cross-sectional images to the *en face* image.

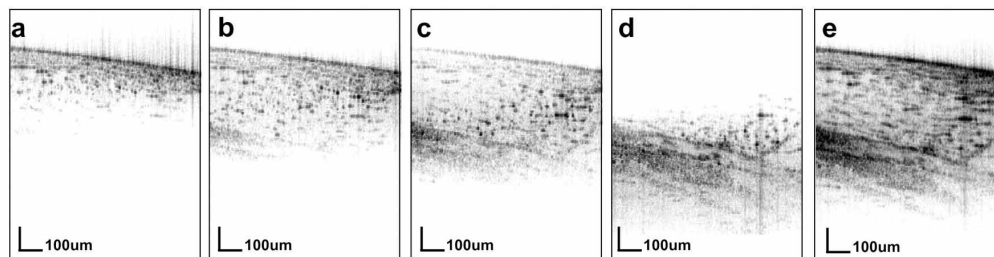


Fig. 12. African frog tadpole (*Xenopus laevis*) *in vivo*. Small region near the spine. a-d. OCT images with different depths of focus; e. Fused image showing cellular structure.

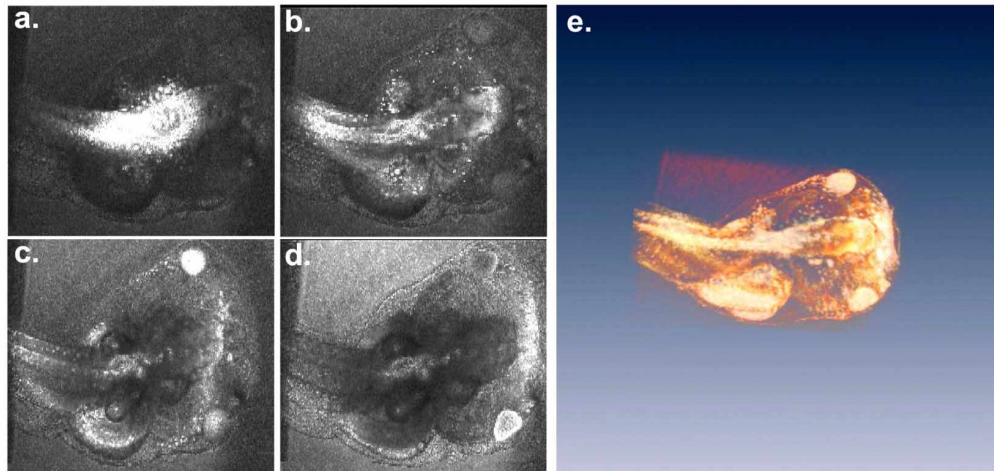


Fig. 13. (1MB movie) Three-dimensional, volumetric *in vivo* imaging of an African frog tadpole (*Xenopus laevis*) using swept source OCT. Left: Four integrated *en face* OCT projections reconstructed from the three-dimensional OCT data sets measured for four different depths of the focal plane. Right: Movie demonstrating volume rendering of the entire tadpole.

Figs. 11(a-d) also show that good contrast is achieved over a depth range larger than the confocal parameter. This occurs because OCT has high detection sensitivity and OCT images are displayed with a logarithmic grey scale. Figure 12 shows high magnification C-mode imaging. The first images (Fig. 12(a-d)) show the same region imaged with four different depths, obtained by axially translating the focal depth of the main objective. After fusing the four OCT images, the combined image (Fig. 12(e)) spans a dimension of 0.6 mm axial x 0.75 mm transverse. The high resolution reveals a granular appearance caused by the cellular structure.

With an effective axial scan rate of 16 kHz, corresponding to a frame rate of 32 frames per second for 512 transverse pixel images, using 4 different focal depths, high speed OCT imaging using swept source/Fourier domain detection can acquire 8 extended depth of field images per second. In integrated OCT/OCM applications, where the large numerical aperture of the objective supports only a limited depth of field, this three-dimensional zone focusing method, combined with the high speed, swept source OCT imaging will enable large areas to be imaged. The high acquisition speed of swept source OCT provides powerful advantages for three-dimensional optical coherence tomography and optical coherence microscopy imaging. By acquiring large, three-dimensional data sets in relatively short amounts of time, it is possible to generate arbitrary transverse and *en face* views over the whole sample. Individual cross-sectional OCT images or *en face* OCM or confocal microscopy like images can be generated and precisely registered with respect to the three-dimensional data set. Arbitrary images can be reconstructed using post processing of the three-dimensional data set.

Fig. 13 shows an example of a three-dimensional data set which covers the entire *Xenopus laevis* tadpole. Four sets of three-dimensional OCT data were collected with different axial positions of the focal plane of the objective. In order to perform an OCT reconstruction of the entire tadpole (Fig. 13), the OCT scanning range was extended to cover an area of 5 mm x 5 mm. A total of 4 data sets with 150 x 512 x 400 points (after recalibration before zero padding) were acquired in approximately 25 seconds. Therefore, this type of imaging can only be performed on anesthetized or immobilized *in vivo* specimens or on *ex vivo* specimens. Higher speed swept laser sources will improve imaging speeds, however three-dimensional imaging will remain challenging due the extremely large amounts of data. The movie (Fig. 13(e)) demonstrates three-dimensional volume rendering of the tadpole obtained by fusing four, three-dimensional OCT data sets. Figure 13 a-d shows four

OCT “confocal” images which are obtained by summing the reconstructed *en face* planes from the four consecutive OCT three-dimensional data sets. These imaging protocols provide an extended axial depth of field while maintaining high spatial resolutions in the axial as well as in the transverse directions.

5. Conclusion

In this study we demonstrate a compact, frequency swept light source at 1300 nm for high speed, three-dimensional, swept source OCT imaging. The laser achieves an effective axial scan rate of 16 kHz and an instantaneous coherence length sufficient for a 3 mm depth range for OCT imaging. Sensitivities as high as 109 dB have been achieved. The bandwidth of the wavelength sweep covers 133 nm full width and an axial resolution of $\sim 10\ \mu\text{m}$ in tissue was achieved. For a small voxel size, the transverse resolution was set to be $4.5\ \mu\text{m}$.

High speed imaging protocols for three-dimensional, C-mode and zone focusing imaging were demonstrated which overcome depth of field limitations to yield high axial and transverse resolutions with extended depth ranges. *En face* images, similar to optical coherence microscopy (OCM) images, where depth gating is provided by the coherence gate, can be generated from the three-dimensional data sets. Furthermore, *en face* images, similar to those produced by confocal microscopy, can be generated by summing the signals in the axial direction. These imaging protocols combine the functionality of optical coherence tomography with optical coherence microscopy and confocal microscopy in a single instrument. High speed, swept source OCT using new frequency swept laser sources promises to enable a wide range of new imaging protocols which can achieve three-dimensional imaging with improved image resolutions and depth of field.

Acknowledgments

We would like to acknowledge scientific contributions and helpful advice from Tony Ko, Pei-Lin Hsiung, Vivek Srinivasan and Mariana Carvalho. Alex Cable acknowledges support from Michael Larsson of Thorlabs AB Sweden, and Egbert Krause of Thorlabs GmbH Germany. M. Wojtkowski is visiting from the Institute of Physics, Nicholas Copernicus University, Torun, Poland. This research was sponsored in part by the National Science Foundation ECS-0119452, BES-0119494 and BES-0522845, National Institutes of Health R01-CA75289-08 and R01-EY11289-20, the Air Force Office of Scientific Research FA9550-040-1-011 and FA9550-040-1-0046, and the German Research Foundation (DFG) Hu 1006/1-1.